RSC Advances

PAPER

View Article Online
View Journal | View Issue

Cite this: *RSC Adv.*, 2026, **16**, 17599

Enhanced Ni^{2+}/Ni^{3+} redox activity in dopant-free nickel-based metal–organic framework for sensitive electrochemical detection of methanol in beverages

D. Arunkumar[c] and G. Lakshmi Priya *[ab]

This work presents a dopant-free nickel-based metal–organic framework (Ni-MOF) electrode revealing enhanced Ni^{2+}/Ni^{3+} redox action for the sensitive electrochemical detection of methanol at room temperature. The scientific interest in volatile organic compounds (VOCs) detection has been significant because of its relevance in the prevention of adulteration-related intoxication. The differences in VOC levels in the human body are valuable predictors of underlying pathophysiological processes and are linked to the identification and monitoring of numerous diseases. A dopant-free Ni-MOF was synthesized in the current study, and its structural and morphological properties were thoroughly characterized with X-ray diffraction (XRD), Fourier-transform infrared spectroscopy (FTIR), Field-emission scanning electron microscopy (FESEM), High-resolution Transmission electron microscopy (HRTEM), and X-ray Photoelectron Spectroscopy (XPS). The electrochemical properties of the synthesised Ni-MOF material were investigated using a glassy carbon electrode as the working electrode. The VOC sensor based on the Ni-MOF material revealed a high analytical performance with a low LOD of 0.5 μM and a high sensitivity of 144.22 μA μM^{-1} cm^{-2} with a linear range from 0.5 to 11 μM. These findings illustrate that the Ni-MOF material would be a viable electrochemical sensing platform for VOCs. The sensor allows indirect detection of methanol in real samples, such as natural and artificial beverages. The recoveries were 95–107% with spiked sample analysis, which showed excellent analytical reliability and a low degree of matrix effects. In general, the proposed work demonstrates the possibilities of applied methanol monitoring in food and drink safety sectors, supporting human health protection.

Received 24th January 2026
Accepted 19th March 2026

DOI: 10.1039/d6ra00638h

rsc.li/rsc-advances

1. Introduction

Volatile organic compounds (VOCs) are organic compounds that readily evaporate at room temperature and have both natural and anthropogenic sources.[1] These substances are significant sources of atmospheric pollution and pose risks to environmental quality and human health. Industrial activities, automotive emissions, power production, agricultural and food-processing processes, and household items are the major contributors to VOC emissions and, thus, impact both indoor and outdoor air quality.[2,3] VOC pollutants are now common in urban and rural areas due to rapid industrialization and urban growth. In addition to air pollution, VOCs are increasingly recognized as key contaminants in the water and soil systems, and as key tools in medical diagnostics to assess health effects and potential outcomes.[4–6] Excessive exposure to high VOC levels may undermine the immune system and harm the body's healthy organs, such as the liver, kidneys, the brain, and the lungs.[7,8] Some of the common VOCs are acetone, ethanol, isopropyl alcohol, dimethyl formamide, chloroform, and methanol. The VOCs are also metabolic by-products, and are found in breath, sweat, urine, and feces, so they have great potential as healthcare biomarkers.[9] Volatile organic compounds (VOCs) have the ability to cause significant health risks, with methanol being a compound that poses a serious health risk. While small amounts of methanol, *i.e.*, less than 25 mg dL^{-1}, may naturally occur in fruits, fruit juices, and fermented products, such small amounts of methanol are not toxic. However, when larger amounts of methanol, especially from adulterated and improperly processed beverages, are ingested, serious health consequences may arise. Blood methanol levels above 25 mg dL^{-1} require medical attention, whereas 60–100 mg dL^{-1} may cause serious toxicity, including visual impairment. Moreover, extremely high amounts of methanol, *i.e.*, 150–620 mg dL^{-1}, may cause life-threatening poisoning, including death.

[a]*Centre for Advanced Materials and Innovative Technologies, Vellore Institute of Technology, Chennai 600127, India. E-mail: lakshmipriya.g@vit.ac.in*

[b]*School of Electronics Engineering, Vellore Institute of Technology, Chennai 600127, India*

[c]*School of Advanced Sciences, Vellore Institute of Technology, Chennai 600127, India. E-mail: arunkumar.d2023a@vitstudent.ac.in*

Methanol is metabolized to formaldehyde and formic acid in the human body, leading to the occurrence of metabolic acidosis and severe damage to vital organs, primarily the nervous system and the eyes. Excessive or long-term exposure can cause permanent blindness, or cause severe disease, or death.[10] The after-effects of poisoning by methanol are not only imaginary; they are a common all-over-the-world tragedy.[11] Such accidents are usually due to bootleg alcohol that is made in illegal plants. The issue reached its highest point during the COVID-19 pandemic, during which harmful misinformation spread the idea that consuming high-strength alcohol would help prevent the illness. This caused almost 6000 cases of toxicity and 800 deaths within only several months of 2020.[12,13] The lack of water has more recently been regarded as a contributor to a tragic event in Kallakurichi district, Tamil Nadu, India, in 2024 that claimed 68 reported lives because of the consumption of methanol-contaminated alcohol. These repeated cases create significant loopholes in the safety monitoring and enforcement of regulations. As such, the accurate monitoring of methanol is highly essential, especially in industrial settings where it is extensively applied as a solvent, fuel additive, or chemical feedstock. Besides that, high-quality control in spirit drinks is necessary to avoid poisoning caused by adulteration.[14]

The creation of a stable and convenient methanol sensor is not a scientific ambition anymore, but an essential need to reduce further life loss. Various analytical methods, such as the gas chromatography-mass spectrometry (GC-Mass spectrometry) technique, high-performance liquid chromatography (HPLC), chemiresistive sensors, and electrochemical methods, have been utilized to detect VOCs.[15] Among them, electrochemical sensing techniques have received much interest because of their high sensitivity, low detection limits, low cost, simplicity, and the capability of real-time measurements.[16] These methods offer measurable current–voltage (*I–V*) responses of redox interactions at the electrode-analyte interface, thus allowing their prompt and dependable identification. Most recent studies have investigated a diverse array of electrochemical detection materials to detect methanol, and they include metal oxides, polymer-composite materials, carbon nanomaterials, as well as hybrid nanostructures. Whereas metal oxide-based sensors have shown encouraging performance, weaknesses include low selectivity, low surface area, and stability during operating conditions are some of the weaknesses. Here, metal–organic frameworks (MOFs) have become good candidates in sensing applications. MOFs are crystallized porous solids that consist of metal ions or clusters coordinated with organic linkers, which provide very large surface areas (1000–10,000 $m^2\ g^{-1}$), tunable pore sizes, and large active sites.[17,18] The above properties make MOFs very useful in catalysis, gaseous storage, gas separation, biomedical, wastewater treatment, and chemical sensing applications.[19,20]

Recent literature has also examined numerous material platforms of electrochemical detection of methanol and related volatile organic compounds. A copper-based metal–organic framework (Cu-BTC) functionalized carbon paste anode has been claimed to detect methanol electrochemically and is reported to show excellent sensitivity and capability to be used in real-time to analyze alcoholic drinks like mescal and aguardiente.[21] Polymer-based sensing materials with coordination polymers ($Ni(4,40\text{-bby})(H_2O)_4](6\text{-Onic})_2$) have also been reported, in which nickel-polymeric and cobalt-polymeric structures of 4,4′-bipyridine, and 6-hydroxynicotinic acid were shown to electro-catalyze methanol oxidation. It was found through comparative analysis that the nickel-based coordination polymer had better electrochemical activity for methanol sensing than its cobalt counterpart.[22] Graphene, titanium dioxide, and silver nanoparticles hybrid nanocomposite electrodes have been designed to improve the performance of sensing devices because of the synergistic effect. Graphene-TiO_2-Ag-based electrodes have been shown to be highly sensitive, stable, and exhibit high electrochemical responses to VOCs such as formaldehyde in food-related samples.[23] In another work, composite materials that were to be used on fluorine-doped tin oxide electrodes were produced using nickel oxide, zinc oxide, polyaniline, and carbon nanotubes (NiO–ZnO/PANI-CNT). These hybrid frameworks had a better rate of electrical conductivity, huge efficient surface area, and good sensitivity to electrochemical methanol detection, and they proved to be successful in real-time analysis of fuel samples.[24] The metal oxide nanostructures obtained by MOF derivation have also drawn attention because of their improved catalytic and charge-transfer actions. NiO@CuO nanostructures derived as porous Ni-MOFs have been explored as sensors of hydrogen gas in high operating temperatures (typically around 150 °C), due to their p-type semiconducting properties, high surface area, and well-dispersed metal content. These properties add to high sensing functionality over conventional metal oxide materials.[25]

Ni-MOFs have also been of growing interest for electrochemical sensing due to their inherent redox activity, structural stability, and controllable porosity. Past experiments have demonstrated that the Ni-MOFs can be modified and optimized in structure to enhance charge-transfer properties and electrochemical activity.[26] MOFs have been investigated in electrocatalysis in recent years, and transition metal-based MOFs have been a research hotspot because of their relatively high conductivity and rich redox activity.[27,28] Ni-MOF nanostructures, such as nanosheet arrays, have also been shown to exhibit efficient electrochemical catalysis and desirable electron transport in alkaline media, which highlights their prospects in their application to electrochemical processes.[29] MOF-based nanoarrays have also been used as flexible microelectrodes for sensitive detection of target analytes in aqueous systems and have shown high stability in real samples.[30,31]

Most reported sensing platforms are based on composite or hybrid materials to increase performance. However, the use of a pure Ni-MOF framework, without any secondary metal species, metal oxides, polymers, or carbon-based species added, for electrochemical methanol detection has not been extensively investigated. To address this research gap, the current study presents the preparation of a pure Ni-MOF-modified glassy carbon electrode (GCE) for sensitive electrochemical detection of methanol. Ni-MOF was synthesized and fully characterized through X-ray diffraction (XRD), Fourier-

transform infrared spectroscopy (FTIR), field-emission scanning electron microscopy (FESEM), high-resolution transmission electron microscopy (HR-TEM), and X-ray photoelectron spectroscopy (XPS). Cyclic voltammetry (CV), differential pulse voltammetry (DPV), and electrochemical impedance spectroscopy (EIS) were used to determine the electrochemical performance of the Ni-MOF-modified GCE. The sensor parameters, such as sensitivity and limit of detection (LOD), were measured in a standard redox electrolyte system. The sensing platform developed shows a sensitive and reliable method of methanol detection in real samples, such as natural and artificial beverages, and could be used for food safety and human health protection.

2. Experimental section

2.1 Materials and methods

The metal precursor and the organic linker employed in the synthesis of the nickel-based metal–organic framework (Ni-MOF) were nickel(II) chloride hexahydrate ($NiCl_2 \cdot 6H_2O$, Merck) and terephthalic acid (benzene-1,4-dicarboxylic acid, $C_8H_6O_4$, Sigma-Aldrich), respectively. *N*, *N*-Dimethylformamide (DMF) was used as the reaction solvent. The volatile organic compounds (VOCs) used were methanol (CH_3OH), acetone (C_3H_6O), propanol (C_3H_7OH), isopropyl alcohol (2-propanol, C_3H_8O), ethanol (C_2H_6O), formaldehyde (CH_2O) and butanol ($C_4H_{10}O$). The supporting electrolytes were potassium chloride (KCl), potassium ferricyanide ($K_3[Fe(CN_6)_6]$), and potassium ferrocyanide ($K_4[Fe(CN_6)_6]$). The phosphate-buffered saline (PBS) was received in analytical-grade form and was not purified. Deionized (DI) water was employed to prepare all aqueous solutions.

2.2 Synthesis of nickel-based metal–organic framework (MOF)

The synthesis of Ni -TPA was performed using a straightforward solvothermal procedure. In short, a homogeneous solution of terephthalic acid (TPA, 0.16 g) and nickel(II) chloride hexahydrate ($NiCl_2 \cdot 6H_2O$, 0.21 g) was prepared by dissolving the reagents in *N*, *N*-dimethylformamide (DMF, 20 mL) and stirring at 500 rpm at room temperature for 20 min. 50 mL Teflon-lined stainless-steel autoclave was filled with the mixture and heated at 120 °C for 24 hours. Once the reaction was complete, the autoclave was left to cool to room temperature. The green precipitate was obtained and washed with ethanol and deionized (DI) water several times to remove precursors and residual solvent from the reaction. The product was then vacuum-dried at 100 °C overnight to produce the final Ni-TPA powder. The schematic representation of the dopant-free Ni-MOF synthesis is presented in Fig. 1.

3. Results and discussions

3.1 X-ray diffraction (XRD) analysis

XRD analysis was conducted to identify the crystal phases of the Ni-BDC(1,4-benzenedicarboxylic acid) MOF formed, and the results are shown in Fig. 2(a). The XRD pattern is sharp and strong with diffraction peaks indicating the high purity and crystalline phase of the sample. It is highly pure and well-defined in the crystalline phase. Each of the observed peaks

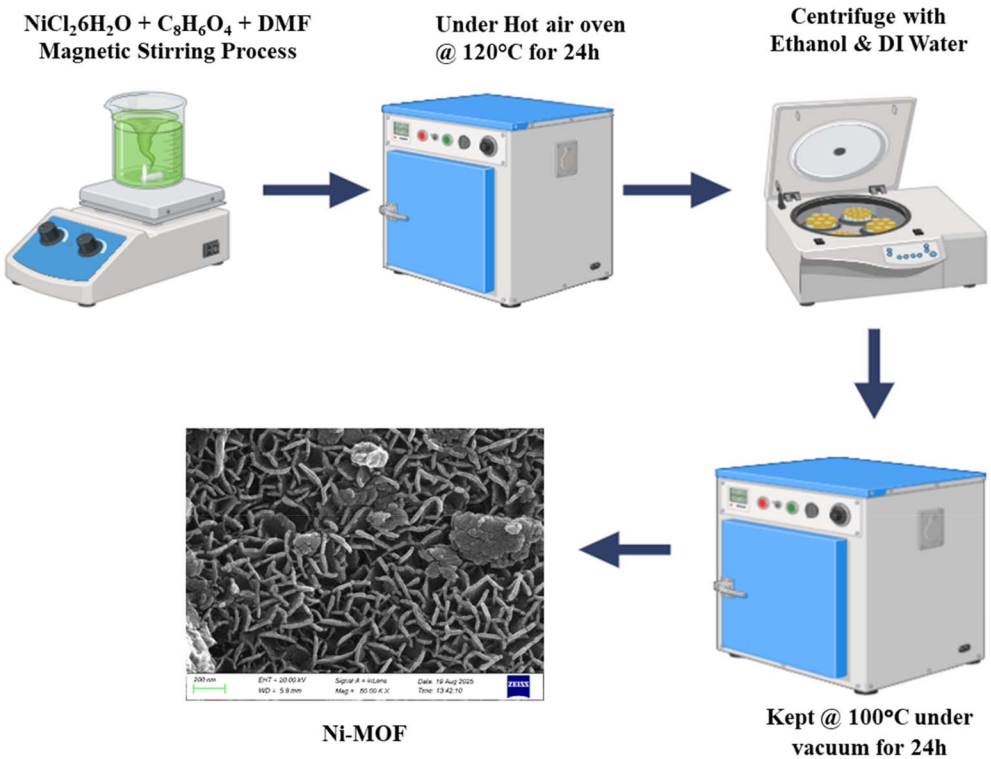

Fig. 1 Schematic presentation of the dopant-free Ni-MOF synthesis process.

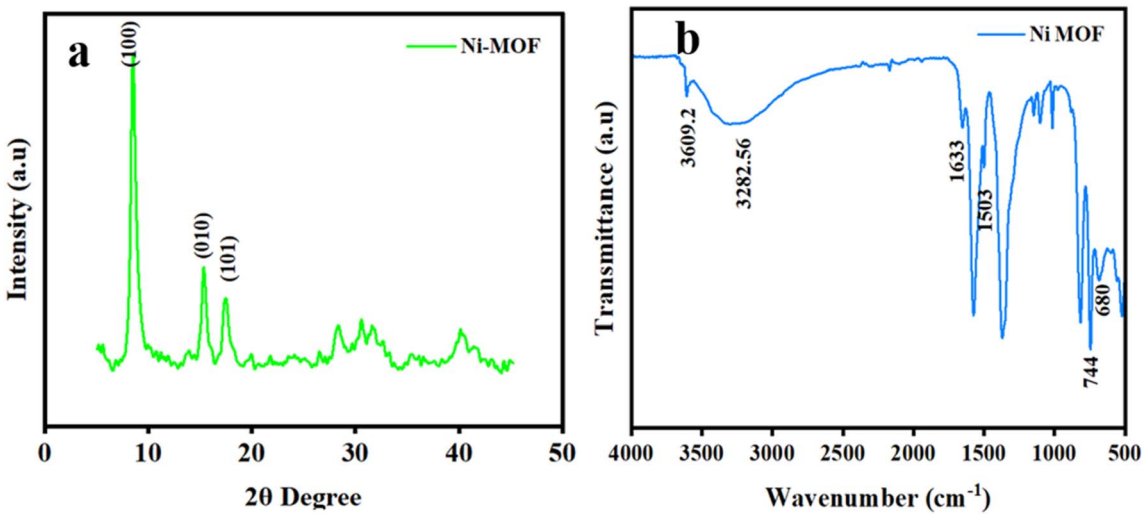

Fig. 2 (a) XRD Pattern of Ni-MOF, (b) FTIR-spectrum of Ni-MOF.

was close to the (CCDC database No: 638866 with significant peaks) at 2θ = 8.3°, 15.4°, and 17.2°, displaying excellent consistency with the standard. The synthesized Ni-MOF was analyzed by XRD to verify the successful formation of the crystalline framework, as reported in the literature. The characteristic peaks in the diffraction pattern are similar to those of Ni-MOF structures reported in previous research, showing that the required crystalline phase has formed. The obtained diffraction peaks also confirm that Ni-MOF has been successfully synthesized. Using the Scherrer equation (eqn (1)), the mean crystallite size (D) was determined as 13 nm, which is shown in Fig. 2(a). The XRD pattern displays the expected diffraction peaks, confirming the formation of the Ni-MOF.[32,33]

$$D = \frac{K\lambda}{\beta \cos\theta} \quad (1)$$

where K represents the shape factor, λ is the Cu Kα wavelength, β is the full width at half maximum (in radians), θ is the Bragg diffraction angle (in degrees).

3.2 Fourier transform infrared (FT-IR) spectroscopy

Fig. 2(b) analysis: infrared Fourier transform is an effective method for identifying functional groups in materials. As shown in the FTIR spectrum (Fig. 2(b)), Ni-MOFs exhibit molecular vibration modes related to the –COO–, OH–, CH, as well as O–Ni–O bonds.[34] The Ni-MOF sample shows a substantial peak at 3602 cm^{-1}, which results from the O–H vibrations of water molecules interacting with a carboxylate group. In contrast, other peaks correspond to aromatic ring vibrations at 1633, 1503, 744, and 680 cm^{-1}. FT-IR sample of Ni-MOF shows a strong peak at 3602 cm^{-1}, which is explained by the presence of O–H stretching bands related to hydrogen-bonded hydroxyl groups in the case of interaction with carboxylate groups. Other typical characteristic peaks at 1633, 1503, 744, and 680 cm^{-1} are aromatic ring vibrations of the organic linker. These interactions are involved in the framework of hydrogen bonding. Thus, the measured –OH addressing is more strongly associated with intramolecular hydrogen bonds within the MOF framework than with physically adsorbed water molecules. The peak at 3282.56 cm^{-1} is attributed to the para-aromatic CH mode.[35] The bands at 1633 and 1503 cm^{-1} indicate the asymmetric and symmetric stretching vibrations of the carboxyl groups, respectively. In contrast, the peaks at 744 and 680 cm^{-1} represent O–Ni–O bond vibrations, consistent with earlier research findings. These consequences confirm the successful synthesis of Ni-MOF. Furthermore, there is also a slight shift in the peaks associated with the vibrations of –COO–, OH–, aromatic CH groups, in association with O–Ni–O interactions in Ni-MOF.[36]

3.3 Scanning electron microscopy (SEM) analysis of Ni-MOF and energy dispersive X-ray (EDX) spectrum

The Ni-MOF has a highly porous structure, as shown in the FESEM image in Fig. 3(a), with pores larger than several hundred nanometers. The high-resolution FESEM image provides evidence that the nano-flower morphology is produced by the smooth and densely packed growth of Ni-MOFs, in which the 2D nano-flowers are distributed unevenly on the Ni-MOF surface. Fig. 3(b) also demonstrates the setting of the Ni-MOF nanoflower and the high-resolution image,[36] consistent with the existing literature survey.

It is important to note that no other elemental signals were observed in the EDX spectrum, confirming the dopant-free character of the Ni-MOF and the absence of secondary phases or foreign elements. The uniform distribution of Ni, C, and O throughout a study area of about 2.5 μM also indicates uniform composition and framework structure purity. The fine structural features of the Ni-MOF are observed in Fig. 3(d), and the individual image of the elements is shown in Fig. 3(e, g and h), where the spatially uniform distribution of Ni, C, and O is quite apparent. Energy-dispersive X-ray (EDX) spectroscopy, which was combined with elemental mapping, was used to analyse the elemental composition and spatial distribution of the synthesised Ni-MOF. As indicated in Fig. 3(d), the elemental maps indicate the evenly distributed nickel (Ni), carbon (C), and oxygen (O) in the framework. The EDX spectrum also confirms the existence of these elements, with atomic percentages of C

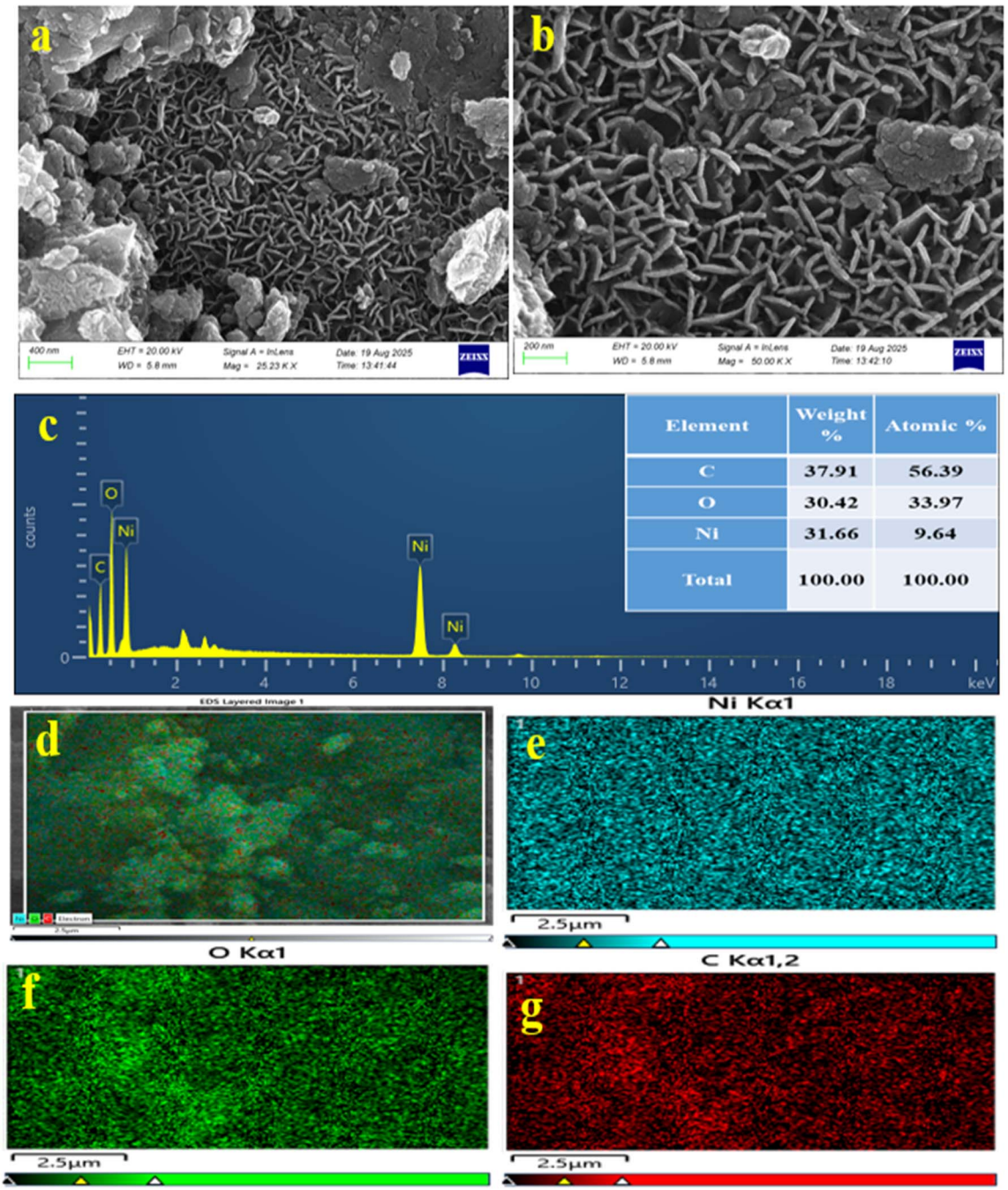

Fig. 3 (a and b) FESEM images of Ni-MOF, (c) energy dispersive X-ray spectrum of Ni-MOF, (d) overall element mapping, individual element mapping of (e)Ni, (f) O, (g) C.

(56.39%), O (33.97%), and Ni (9.64%), as given in the inset of Fig. 3(c). Together, the EDX and elemental mapping are absolute indications of a successful synthesis of pure, dopant-free Ni-MOF that is essential for reproducible and reliable electrochemical sensing behaviour.

3.4 High resolution transmission electron microscopy (HRTEM)

The HR-TEM images of the synthesised Ni-MOF are shown in Fig. 4(a), which are obtained in the scale bar of 10 nm. This shows that the contrast distribution is uniform without clear fringes between the lattice, which confirms that the Ni-MOF framework is relatively low crystalline or partially amorphous. This property is a typical characteristic of metal–organic framework materials because of the coordination of metal ions and organic ligands. The formation of thin sheet-like and layered structures is clearly visible in Fig. 4(b) and (c) with a scale bar of 50 nm and 100 nm. These irregular 2D nanosheets seem to be linked together and a little aggregated to take the form of a porous network structure and particle size of 18 nm. Fig. 4(d) denotes the Selected Area Electron Diffraction (SAED)

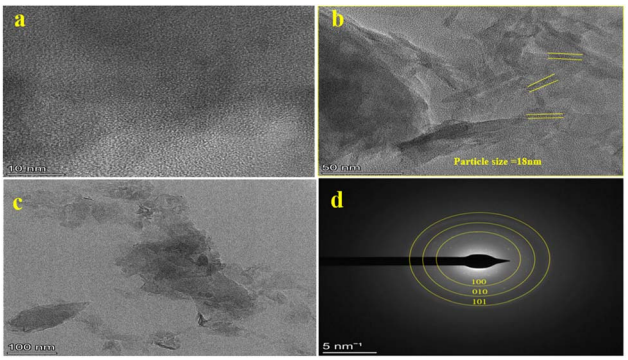

Fig. 4 (a–c) HR-TEM images of Ni-MOF (d) HR-TEM SAED image of Ni-MOF.

image of the *d*-spacing corresponding to the (100) planes of a crystalline phase, which is in good agreement with XRD results. The ability of such a morphology to offer too much surface area and too many open active sites is beneficial to electrochemical reactions and to enhance the efficiency of electron transfer in the course of sensing. The formation of the Ni-MOF nanostructure is thus successful as indicated by the HR-TEM results.[28,36]

3.5 X-ray photoelectron spectroscopy (XPS)

To determine the chemical composition and oxidation state of the surface structure of the synthesised Ni-MOF, X-ray photoelectron spectroscopy (XPS) was used. Fig. 5(a) indicates the existence of nickel (Ni), carbon (C), and oxygen (O), and no other elemental signal was recorded, which shows the dopant-free character of the Ni-MOF structure.[37] The fine-resolution Ni 2p spectrum (Fig. 5(b)) has two typical spin–orbit doublets of binding energy about 855.6 eV (Ni $2p_{3/2}$) and 873.2 eV (Ni $2p_{1/2}$), which are characteristic of Ni^{2+}. The satellite peaks of 861.4 eV and 880.1 eV also support the evidence of the divalent oxidation state of nickel in the MOF structure. Notably, these Ni^{2+} active-centres are very important in the electro-oxidation of methanol, in which reversible redox changes (Ni^{2+}/Ni^{3+}) assist in the adsorption, activation, and electron-transfer of methanol molecules at the electrode–electrolyte interface. The C 1s spectrum at the high-resolution (Fig. 5(c)) was deconvoluted into two peaks at 284.8 eV and 288.5 eV, which were identified as C–C/C=C bonds and C=O/C–N bonds, respectively, indicating the presence of organic linker moieties in the framework. These organic linkers provide structural stability and facilitate efficient charge transportation during electrochemical sensing.[38] The O 1s spectrum (Fig. 5(d)) indicates that there are many

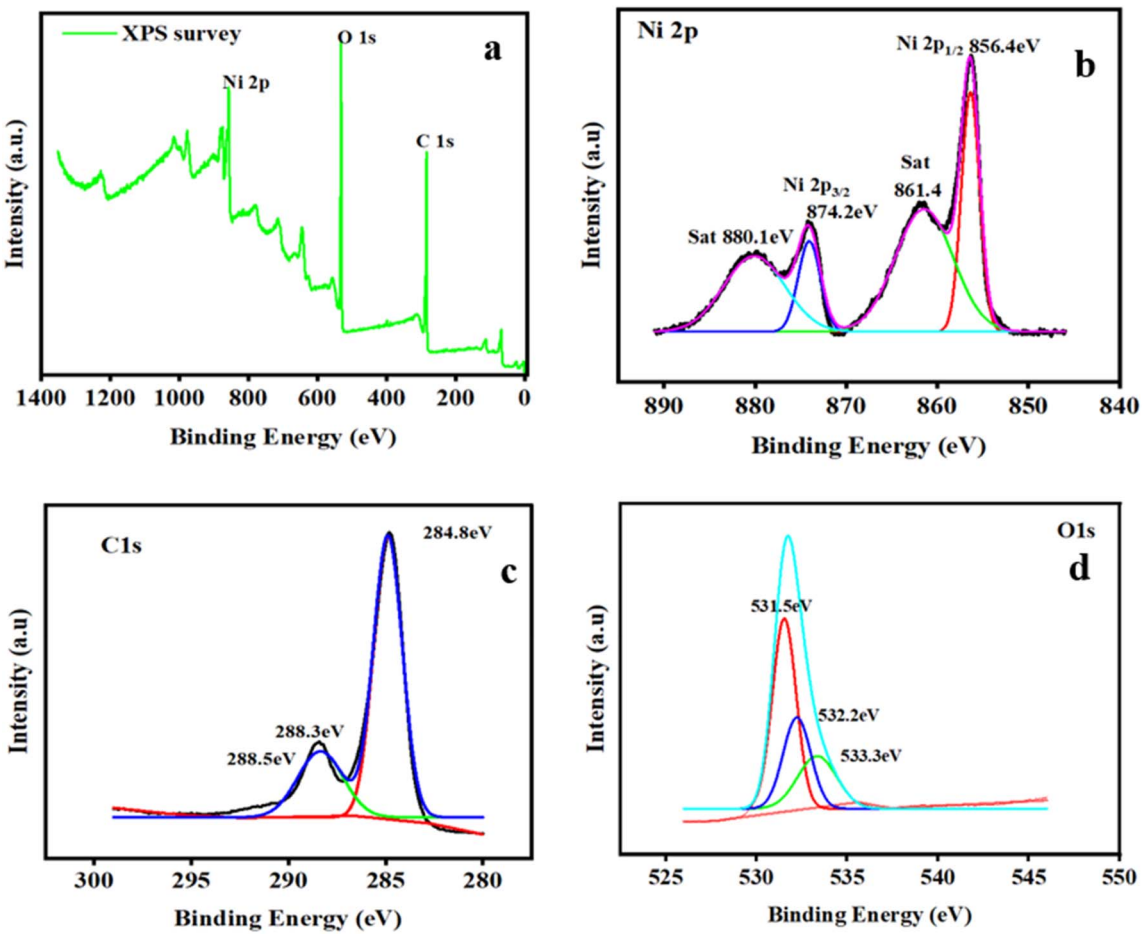

Fig. 5 (a) XPS spectra Ni-MOF survey, (b) Ni 2p, (C) C 1s, (d) O 1s samples.

oxygenated environments, such as Ni–O, C–O, and C═O bonds, which serve to offer oxygen-based coordination sites that increase methanol adsorption and stabilization of intermediates in the oxidation process.[39] The XPS findings therefore provide support to the elemental composition, oxidation states, and chemical bonding of the Ni-MOF, and the prevalence of surface-accessible Ni^{2+} redox-active sites (along with the absence of dopant groups in the framework) in the formation of the effective electrochemical nickel oxidation and sensitive electrochemical detection of methanol.[40]

4. Electrochemical performance of Ni-MOF modified GCE for methanol sensing

The electrochemical measurements were conducted with a PalmSens (PSTrace 5.10) electrochemical workstation, which was operated in a traditional three-electrode setup, where the counter electrode was a platinum (Pt) wire, the reference electrode was an Ag/AgCl electrode, and a glassy carbon electrode (GCE) was the working electrode. To assess the electrochemical performance of the electrodes, cyclic voltammetry (CV), differential pulse voltammetry (DPV), and electrochemical impedance spectroscopy (EIS) were used. Experiments were done on the sensing of methanol in an electrolyte containing 5 mM $[Fe(CN)_6]^{3-/4-}$ and 0.1 M KCl. To improve the electrocatalytic activity and sensing application of the GCE surface, the synthesized Ni-MOF was deposited. Fig. 6(a) demonstrates the CV responses of the Ni-MOF modified GCE in different electrolytes, including PBS, KCl, $[Fe(CN)_6]^{3-/4-}$, PBS with $[Fe(CN)_6]^{3-/4-}$, and KCl with $[Fe(CN)_6]^{3-/4-}$. Among these, the KCl solution containing $[Fe(CN)_6]^{3-/4-}$ shows significantly improved electrochemical response, indicating a higher electron-transfer activity. Hence, KCl with $[Fe(CN)_6]^{3-/4-}$ is chosen as the active electrolyte medium for further studies of electrochemical methanol sensing.

Fig. 6(b) presents a comparison of the CV response of bare GCE, Ni-MOF-modified GCE, and Ni-MOF/GCE in the presence of 1 μM methanol as analyte under various working conditions. The current response of the bare GCE is higher than that of the Ni-MOF-modified GCE. When Ni-MOF is modified, current is observed to decrease, and this may be explained by the relatively insulating properties of the organic linkers and the limited ability of the redox species to move through the microporous framework. Nevertheless, when 1 0 M methanol is added, Ni-MOF/GCE indicates a significant increase in current response. Ni-MOF modified electrode produces clear redox peaks in the electrolyte, and the current signal is further improved with the

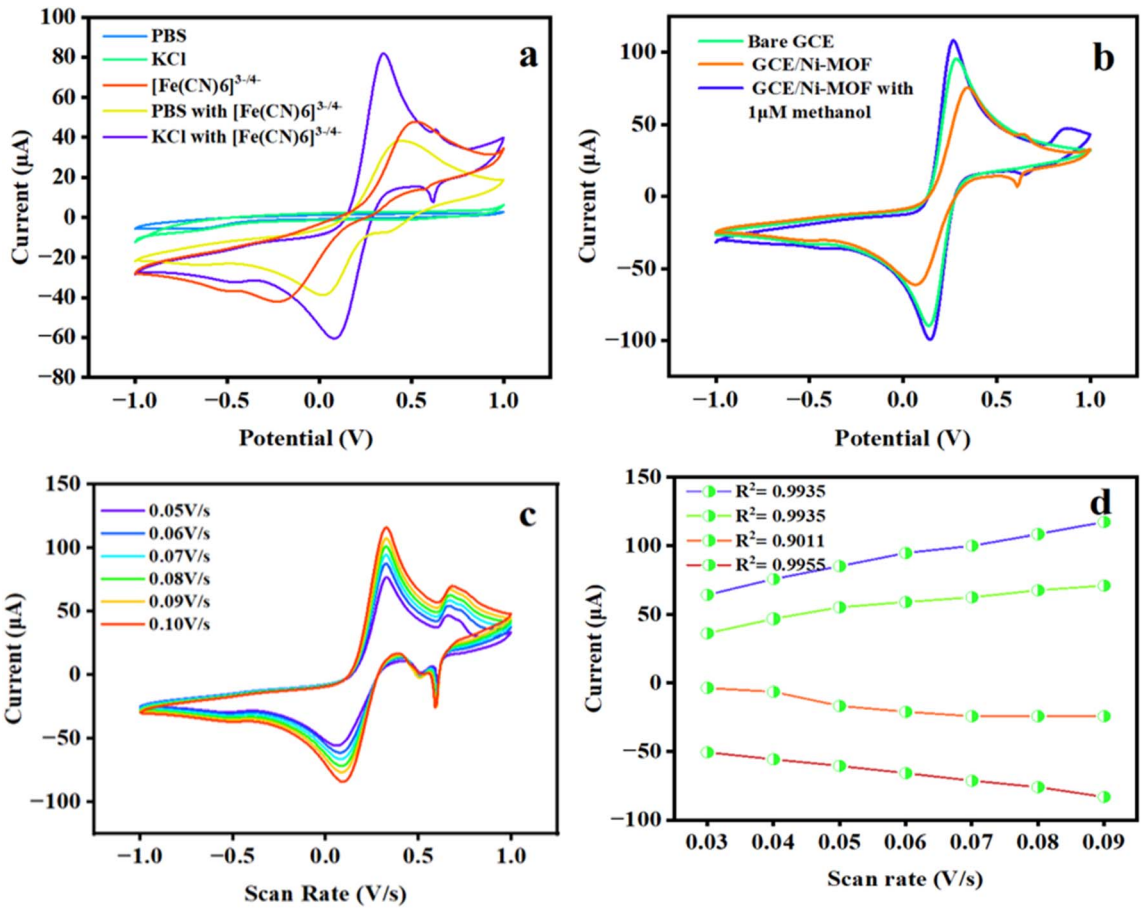

Fig. 6 Cyclic voltammograms of Ni-MOF, (a) for different electrolytes, (b) 0.1 M KCl and 5 mM $[Fe(CN)_6]^{3-/4-}$ as electrolyte using Ni-MOF modified GCE in the presence of 1 μM methanol, (c) for different scan rates, (d) linear calibration fit.

addition of methanol. This phenomenon demonstrates that the Ni-MOF structure enables electrochemical reactions on the electrode surface and is a highly efficient active sensing layer in the detection of methanol.[41]

4.1 Effect of scan rate on the redox kinetics of Ni-MOF

Fig. 6(c) illustrates the scan-rate dependence of the Ni-MOF-modified GCE, which was examined in the presence of 1 μM methanol over a scan-rate range of 0.05–0.10 V s^{-1}. Both cyclic voltammograms have clear oxidation peaks between 0.5 and 1.0 V, which are assigned to the reversible Ni^{2+}/Ni^{3+} redox transition within the Ni-MOF framework. This redox couple is important in catalyzing the electrocatalytic oxidation of methanol, with the Ni^{3+} species being the active catalytic centres, which promote electron transfer between the methanol molecules at the electrode interface. The electrochemical activities are evident in the potential range of −1 to +1 V, where the highest values of currents are recorded, which are proportional to the scan rate, a characteristic of efficient charge transfer over the surface of the Ni-MOF modified electrode. The improved electrocatalytic activity is due to the uniform coverage of the surface by the dopant-free Ni-MOF that offers a high concentration of free Ni^{2+} active sites as well as a conducting pathway for electron transfer.

As Fig. 6(d) indicates, the anodic maximum current is directly proportional to the square root of the scan rate, which validates the assumption that the methanol oxidation reaction is largely diffusion-controlled. This kinetic behaviour is further justified by high values of linear correlation coefficients (R^2 = 0.9935 and 0.9011). It is important to note that the oxidation peak that was recorded as strong at around 0.5 V indicates heavy interfacial contact between the electrode modified with Ni-MOF and the methanol electrolyte, and the electrolyte, which leads to high charge-transfer efficiency and low overpotential applied to oxidize methanol.[42]

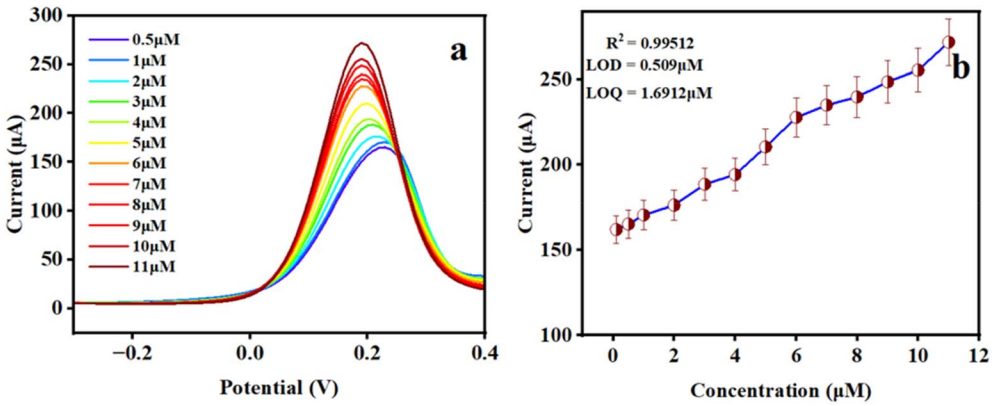

Fig. 7 (a) Differential pulse voltammetry response of Ni-MOF with 0.1 M KCl and 5 mM $[Fe(CN)_6]^{3-/4-}$ electrolyte for various concentrations of methanol, (b) linear relationship plot.

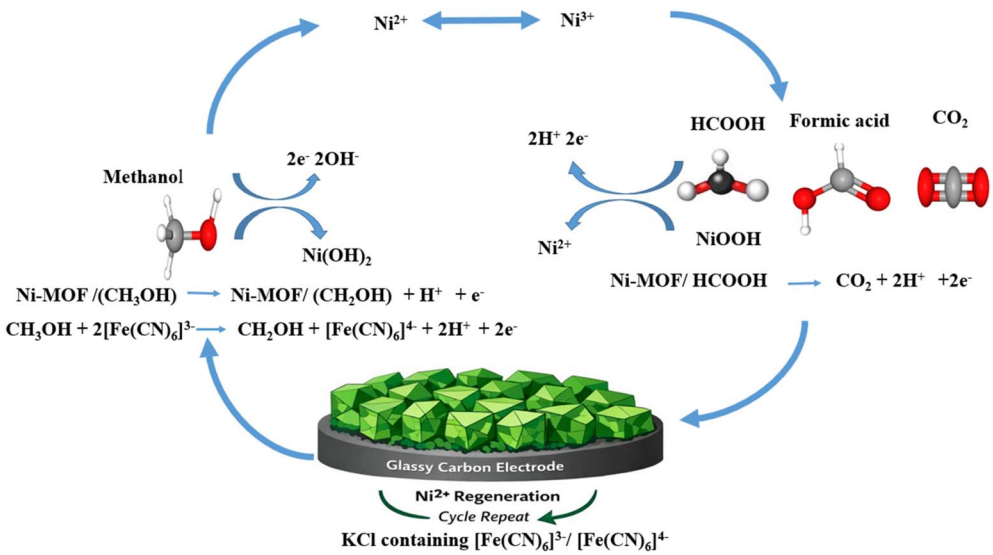

Fig. 8 Dopant-free Ni-MOF electrochemical reaction with indirect methanol oxidation.

4.2 Concentration-dependent electrochemical response

High sensitivity for methanol detection was achieved using differential pulse voltammetry (DPV), as shown in Fig. 7(a). DPV has higher selectivity and sensitivity compared to cyclic voltammetry; therefore, it is highly favourable for the detection of methanol. The effects of pH on the electrochemical response were systematically determined in the range of pH 4–8 in order to optimise the sensor performance. The highest current response was attained at pH 6.5, and thus it was chosen as the best operating condition to be used in the further measurements. The Ni-MOF-modified GCE under these optimized conditions displayed a high level of selectivity and sensitivity toward methanol. Methanol concentrations between 0.5 and 11 μM were measured through DPV, and a linear correlation was established between the concentration of methanol and peak current in the potential range of −1.0 to +1.0 V at a scan rate of 0.05 V s^{-1}. The maximum current (I_n) as depicted in Fig. 7(b) rises gradually with the concentration of methanol, which is an indication of the effective electrocatalytic oxidation within the electrode surface. The slope of the calibration plot was used to determine the sensitivity of the sensor, and the high correlation coefficient ($R^2 = 0.995$) indicates that the reaction between the methanol concentration and the electrochemical response is highly linear. The high linearity allows good quantification of methanol in unknown samples through the calibration curve. The near-unity coefficient of determination is another indication of the precision and repeatability of the sensor developed. Electrochemical reactions that control the oxidation of methanol on the Ni-MOF-modified electrode are summarised in the following eqn (2)–(9), depicting the indirect method for methanol detection,[23,43] and eqn (4)–(9) in Fig. 8.

The oxidized mediator accepts electrons produced from methanol oxidation

$$[Fe(CN)_6]^{3-} + e^- \rightarrow [Fe(CN)_6]^{4-} \quad (2)$$

Electron transfer to electrode

$$[Fe(CN)_6]^{4-} \rightarrow [Fe(CN)_6]^{3-} + e^- \quad (3)$$

Role of the Ferri/Ferrocyanide continuous catalytic redox cycle

$$[Fe(CN)_6]^{3-} \leftrightarrow [Fe(CN)_6]^{4-} \quad (4)$$

Electrocatalytic activity of methanol in 0.1 M KCl and 5 mM $[Fe(CN)_6]^{3-/4-}$

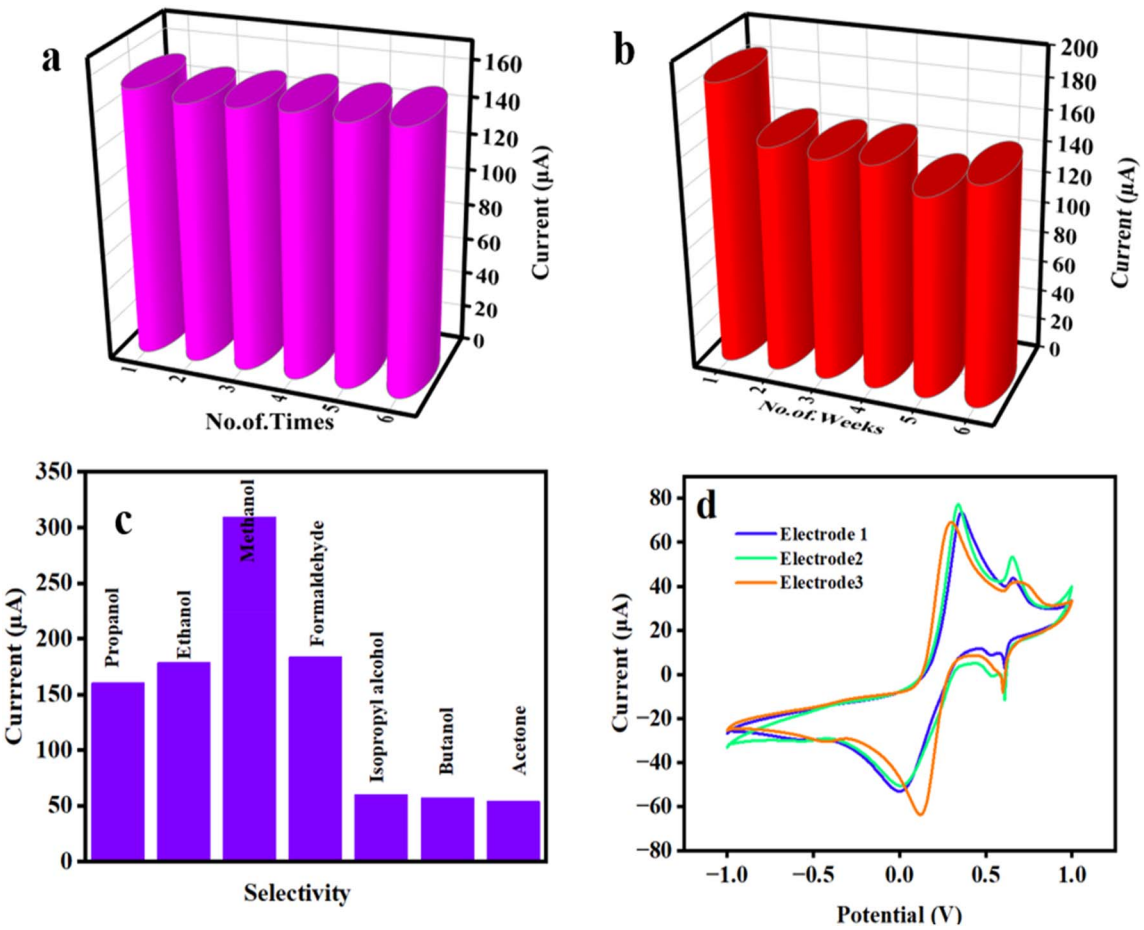

Fig. 9 (a) Repeatability, (b) stability, (c) selectivity, (d) reproducibility studies of GCE modified electrode with Ni-MOF for the sensitive detection of methanol with 0.1 M KCl and 5 mM $[Fe(CN)_6]^{3-/4-}$ as electrolyte.

$$CH_3OH + 2[Fe(CN)_6]^{3-} \rightarrow CH_2OH + 2[Fe(CN)_6]^{4-} + 2H^+ + 2e^- \quad (5)$$

Methanol adsorption with Ni-MOF

$$\text{Ni-MOF} + CH_3OH \rightarrow \text{Ni MOF} / (CH_3OH) \quad (6)$$

$$\text{Ni-MOF} / (CH_3OH) \rightarrow \text{Ni MOF}/ (CH_2OH) + H^+ + e^- \quad (7)$$

$$\text{Ni-MOF}/ CH_3OH_{ads} + H_2O \rightarrow HCOOH + 4H^+ + 4e^- \quad (8)$$

$$\text{Ni-MOF}/ HCOOH \rightarrow CO_2 + 2H^+ + 2e^- \quad (9)$$

The redox couple 0.1 M KCl and 5 mM $[Fe(CN)_6]^{3-/4-}$ is the electron mediator in the sensing system. Ni-MOF offers active sites that can be used as catalysts, on which methanol molecules are adsorbed and oxidized. In this reaction, the electrons produced by the oxidation of methanol are initially moved to $[Fe(CN)_6]^{3-}$, reducing it to $[Fe(CN)_6]^{4-}$. The reduced species further donates electrons to the electrode surface to improve the current that is measured. Thus, catalytic oxidation is caused by Ni-MOF, and the electron transfer is promoted by 0.1 M KCl and 5 mM $[Fe(CN)_6]^{3-/4-}$ couple, to increase the electrochemical signal and sensitivity. This implies that the sensing process is a mediated (indirect) electron transfer and not the direct oxidation.

The lower limits of detection (LOD) and lower limits of quantification (LOQ) were determined using the standard analytical equations.

$$LOD = 3.3\frac{\sigma}{S} \quad (10)$$

$$LOQ = 10\frac{\sigma}{S} \quad (11)$$

where σ is the standard deviation of the blank (baseline noise), and S is the slope of the calibration curve. Sensitivity was calculated using;

$$\text{Sensitivity} = \frac{\text{slope}}{\text{active surface area}} \quad (12)$$

Using eqn (10) and (11), the Limit of detection (LOD) and limit of quantification (LOQ) were determined to be 0.509 μM and 1.6912 μM, respectively, demonstrating the high analytical performance of the developed electrode. The relatively low LOD indicates an increased sensitivity of 144.2274 μA μM^{-1} cm^{-2} for methanol detection, calculated using eqn (12) and is lower than most of the electrochemical sensors that have been reported previously. The low detection limit is an advantage in the sensitive detection of methanol, an important factor in identifying adulteration and maintaining standards in food and beverage products. Moreover, the clearly defined LOQ indicates that the sensor can quantify methanol levels within the investigated range with accuracy and reproducibility, ensuring reliable quantitative analysis of unknown samples. Overall, the LOD and LOQ values demonstrate the appropriateness of the Ni-MOF-modified electrode for sensitive and accurate methanol sensing.[41,44]

4.3 Repeatability, stability, selectivity, and reproducibility studies

Fig. 9(a) and (b) show the repeatability and stability of the Ni-MOF-modified GCE, which are the two most important parameters for assessing the usefulness of the technology in methanol sensing. Repeatability is the sensor's ability to produce consistent results under the same experimental conditions and was evaluated by obtaining repeated electrochemical measurements at a constant methanol concentration. The relative standard deviation (RSD) of the oxidation peak current, a common quantitative measure of repeatability, was less than 5% (3.5%), as confirmed by seven consecutive measurements with a single GCE electrode coated with Ni-MOF.

Further, the stability of the Ni-MOF/GCE was studied by differential pulse voltammetry over six weeks. The electrode was kept in a desiccator at room temperature and run at regular intervals at the optimized pH of 6.5. The sensor maintained a high current response, a steady peak potential, and signal intensity declined by only about 3, 5, and 8%, as indicated in Fig. 9(b). These findings indicate that the dopant-free Ni-MOF-modified electrode is stable for several weeks in detecting methanol.

The selectivity experiment was also conducted in the presence of potential interfering species, such as propanol, isopropyl alcohol, formaldehyde, ethanol, acetone, and butanol, as shown in Fig. 9(c). A strong current response was observed upon methanol addition, and no significant responses were observed with the interfering compounds; thus, the sensor's excellent selectivity for methanol was confirmed.

Finally, reproducibility was assessed using three independently prepared Ni-MOF-modified GCEs, which exhibited nearly identical electrochemical responses, with a low RSD indicating good electrode-to-electrode reproducibility. Fig. 9(d) displays the CV responses of the three electrodes prepared separately, showing consistent performance across them. Overall, these

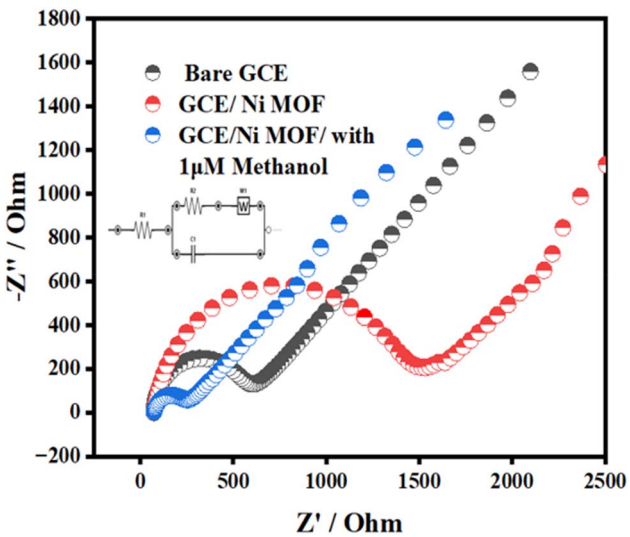

Fig. 10 Nyquist response of the bare GCE, Ni-MOF-modified GCE, and Ni-MOF-modified GCE in the presence of 1 μM methanol.

results verify that the Ni-MOF-based sensor demonstrates reliable, stable, and consistent electrochemical behavior over multiple measurements, different electrodes, and varied experimental conditions.[45]

4.4 Impedance spectroscopy

Electrochemical impedance spectroscopy (EIS) was used to study the charge-transfer behaviour of the prepared electrodes. Fig. 10 shows the Nyquist plots obtained on the bare GCE, Ni-MOF-modified GCE, and Ni-MOF-modified GCE in the presence of 1 μM methanol, at 0.1 M KCl containing 5 mM $[Fe(CN)_6]^{3-/4-}$. The Nyquist plots also show a typical semicircle in the high-frequency region and a linear tail in the low-frequency region across all electrodes.[46] The high-frequency semicircle is due to charge-transfer resistance (R_{ct}) at the electrode–electrolyte interface, and the low-frequency linearity is due to the Warburg impedance, which is caused by the diffusion-limited movement of electrolyte ions. Compared with the bare GCE, the Ni-MOF-modified electrode shows a larger semicircle, implying that R_{ct} is higher due to the MOF framework's inherent resistance to electron transfer. But with the addition of methanol, a sharp decrease in the semicircle diameter is observed, which indicates a significant decrease in R_{ct} and faster interfacial electron-transfer kinetics in the oxidation of methanol.[47] The R_{ct} values of the various modified GCEs are as follows: 1 μM methanol < bare GCE < Ni-MOFs, which indicates that the highest rate of electron transfer and conductivity of Ni-MOF to an interfacial electrochemical reaction is at its optimum in the Bode phase plot. The frequency component near 500 Hz can be attributed to bulk electron transfer.[48] At mild-to-moderate frequencies, the impedance behaviour is consistent with the reduced Ni-MOF, as observed from the Nyquist plot. Resistance values experimentally measured were about 361 Ω for bare GCE, 1415 Ω for the Ni-MOF-modified electrode, and 169 Ω for the electrode with 1 μM methanol.[48] These findings confirm that the pristine Ni-MOF has a higher interfacial resistance; however, its reaction with methanol decreases the total resistance by a significant margin, thus increasing the rate of energy transfer between the electrodes and leading to improved electrochemical characteristics.[49]

Table 1 summarizes the comparative overview of the earlier reported electrochemical sensors for volatile organic compounds (VOC) detection, and specifically the Ni-MOF-based methanol sensor of the present study. The analogy shows that the current sensor has better analytical capability with the low limit of detection. The obtained LOD of 0.5 μM, as well as its sufficiently high sensitivity, confirms the ability of the Ni-MOF sensor to detect methanol in trace amounts. This reduced detection limit of our proposed work allows trace-level detection to be achieved, which is especially significant in food safety surveillance and identification of adulteration in beverage products.

4.5 Real-time methanol detection in beverage samples

The usability of the proposed Ni-MOF methanol sensor was tested on actual beverage samples, comprising a natural and an artificial beverage, with 10 μM methanol added to compare. The

Table 1 Comparison of different VOC detection using the electrochemical method

Electrode material	Technique	LOD (μM)	VOC	References
Cu-BTC[a]	DPV	51	Methanol	21
Ni(4,40-bby)$(H_2O)_4$](6-Onic)$_2$[b]	DPV	0.8	Methanol	22
(TiO_2/Ag) graphene[c]	CV	0.8	Formaldehyde	23
CuO/Cu_2O bulk heterostructure[d]	CV	3.75	Methanol	49
NiO-ZNO/PANI-CNTs[e]	DPV	19.4	Acetone	24
Cu-MOF[f]	DPV	44	Methanol	50
Dopant-free Ni-MOF	***DPV***	***0.5***	***Methanol***	***This work***

[a] Cu-BTC-Cu(II)-BTC metal–organic framework modified carbon paste electrode. [b] Ni(4,40-bby)(H_2O)4](6-Onic)2-Tetraaqua(4,4′-bipyridine-κN) nickel(II) 6-oxonicotinate. [c] (TiO_2/Ag) graphene-titanium dioxide/silver/reduced graphene oxide. [d] CuO/Cu_2O bulk heterostructure-cupric oxide (CuO) and cuprous oxide (Cu_2O). [e] NiO-ZNO/PANI-CNTs-nickel oxide-zinc oxide/polyaniline-carbon nanotube nanocomposite. [f] Cu-MOF-metal–organic frameworks enzyme-based electrode.

Table 2 Analytical performance of the Ni-MOF sensor for methanol detection in spiked beverage samples

Natural beverage				Artificial beverage			
Sample day wise	Spiked (μM)	Found (μM)	Recovery %	Sample day wise	Spiked (μM)	Found (μM)	Recovery %
1	10	9.9	99	1	10	9.9	99
2	10	9.8	98	2	10	1	100
3	10	9.6	96	3	10	10.3	103
4	10	9.7	97	4	10	10.6	106
5	10	9.5	95	5	10	10.5	105

samples were tested under optimised different pulse voltammetry (DPV) conditions.

The values of the added concentration, measured concentration, and the recovery values under the optimized conditions are tabulated in Table 2. The recovery was 95–107%, which is good analytical precision of the electrode. These findings indicate that the sensor offers sensitive trace-level detection across complex beverage matrices as well, and therefore has potential in highly sensitive indirect analysis of methanol in real beverage samples.

5. Conclusion

An electrochemical sensor of methanol detection at room temperature was successfully developed and tested in this study with 0.1 M KCl as a supporting electrolyte and 5 mM $[Fe(CN)_6]^{3-/4-}$ as a redox probe. The analysis of the crystalline phase by X-ray diffraction proved that the Ni-MOF has been formed successfully average crystallite size of about 13 nm. Field-emission scanning electron microscopy has shown a quasi-two-dimensional flower-like Ni-MOF nanosheet structure. The structural integrity and elemental composition of the material were also confirmed by XRD, FTIR, HR-TEM (irregular two-dimensional nanosheets), particle-size distribution (18 nm), FE-SEM, and XPS analyses. Differential pulse voltammetry showed excellent performance in methanol sensing with a low detection limit of 0.5 μM and a sensitivity of 144.22 μA μM^{-1} cm^{-2}. These findings indicate that dopant-free Ni-MOF has potential as an indirect electrochemical sensor for methanol in both natural and artificial drinks. Analyzing real samples showed good recovery rates, which suggests that the proposed dopant-free Ni-MOF modified sensor could be useful for assessing beverage safety and safeguarding human health in practical applications.

Compliance with ethical standards

The manuscript is prepared as per the ethical standards of the journal. There were no Human Participants and/or Animals involved while conducting this study.

Consent for publication

The authors have given consent for publication as per the journal policy.

Author contributions

Arunkumar D: formal analysis, investigation, methodology, software, writing – original draft. Lakshmi Priya G: conceptualization, resources, supervision, validation, writing – original draft, writing – review & editing. All the authors have contributed to the overall paper drafting, extraction of results, and editing work for their respective sections. All authors reviewed the manuscript.

Conflicts of interest

The authors declare that they have no known competing financial interests or personal relationships that could have appeared to influence the work reported in this paper.

Data availability

All relevant data pertaining to this work are mentioned in the manuscript itself.

References

1 M. S. Kamal, S. A. Razzak and M. M. Hossain, *Atmos. Environ.*, 2016, **140**, 117–134.
2 X. Ding, H. Liu, J. Chen, M. Wen, G. Li, T. An and H. Zhao, *Nanoscale*, 2020, **12**, 9462–9470.
3 B. Selvaraj, J. B. Karnam and J. B. B. Rayappan, *Ceram. Int.*, 2023, **49**, 37106–37117.
4 Z. Khatoon, H. Fouad, O. Y. Alothman, M. Hashem, Z. A. Ansari and S. A. Ansari, *ACS Omega*, 2020, **5**, 27645–27654.
5 M. Shooshtari and A. Salehi, *Sensor. Actuator. B Chem.*, 2022, **357**, 131418.
6 M. M. Rahmam, *Sens. Actuators, B*, 2020, **305**, 127541.
7 N. Sharma and R. Kumar, *Inorg. Chem. Commun.*, 2024, **162**, 112224.
8 S. Kailasa, M. Sai Bhargava Reddy, B. Geeta Rani, K. Venkateswara Rao, K. Deshmukh and K. Kumar Sadasivuni, *Inorg. Chem. Commun.*, 2023, **157**, 111420.
9 Y. Feng, L. Wu, Y. Luo, Y. Hao, P. Zhang, R. Zeng and S. Chen, *Talanta*, 2025, **291**, 127858.
10 F. Z. Kashani and M. Mohsennia, *Int. J. Hydrogen Energy*, 2025, **101**, 348–357.
11 M. Tomsia, M. Głaz, J. Nowicka, J. Cieśla, M. Sosnowski and E. Chełmecka, *Toxics*, 2022, **10**(12), 800.
12 K. Sarıbaş, A. A. Akpınar, P. E. Özşeker, Ö. Taşkın, N. R. Dişel and G. F. Devecioğlu, *Ir. J. Med. Sci.*, 2025, 1461–1470.
13 S. A. Hashemi, S. Bahrani, S. M. Mousavi, N. Omidifar, M. Arjmand, K. B. Lankarani, M. Shokripour and S. Ramakrishna, *Anal. Chim. Acta*, 2022, **1194**, 339407.
14 A. A. Kotp, A. Abdelwahab, A. A. Farghali and A. Enaiet Allah, *Int. J. Hydrogen Energy*, 2024, **91**, 506–518.
15 S. Norouzi, H. Alavi-Rad, S. S. Ghoreishi Amiri, R. Yousefi and H. Dehbovid, *Sens. Biosens. Res.*, 2025, **48**, 100809.
16 Z. M. Karazan and M. Roushani, *Electrocatalysis*, 2024, **15**, 110–119.
17 M. Ding, X. Cai and H. L. Jiang, *Chem. Sci.*, 2019, **10**, 10209–10230.
18 K. Y. Shin, L. H. T. Nguyen, H. L. Nguyen, A. Mirzaei, V. N. H. Tran, N. X. D. Mai, N. Q. Tran, W. Oum, E. B. Kim, H. M. Kim, T. B. Phan, T. L. H. Doan, S. S. Kim and H. W. Kim, *Sensor. Actuator. B Chem.*, 2023, **394**, 134425.
19 Y. Xiao, W. Wei, M. Zhang, S. Jiao, Y. Shi and S. Ding, *ACS Appl. Energy Mater.*, 2019, **2**, 2169–2177.

20 F. Wang, J. Hu, Y. Peng, X. Wu, H. Xue and H. Pang, *Adv. Sens. Energy Mater.*, 2023, **2**, 100053.
21 J. A. Cruz-Navarro, L. H. Mendoza-Huizar, V. Salazar-Pereda, C. Romo-Gómez, J. Á. Cobos-Murcia and G. A. Álvarez-Romero, *J. Electrochem. Soc.*, 2022, **169**, 037509.
22 I. Škugor Rončević, M. Buzuk, B. M. Kukovec, V. Sokol, M. Buljac and N. Vladislavić, *Crystals*, 2023, **13**(5), 718.
23 M. Natsir, M. Nurdin, Z. R. Syah, S. D. Astuti, T. Azis, L. O. M. Z. Mulkiyan, L. O. Agus Salim, F. Mustapa, A. Zulfan and M. Maulidiyah, *Surf. Eng. Appl. Electrochem.*, 2024, **60**, 247–255.
24 P. T. Nam, N. T. Thom, V. T. Kieu Anh, H. Le Thanh Nguyen, N. T. Thu Trang, N. T. Hoang, N. Vân-Anh, N. T. Anh, L. V. Hai and T. D. Lam, *RSC Adv.*, 2023, **13**, 36060–36070.
25 S. Shah, S. Hussain, L. Ali, K. Yusuf, R. Kumar, Y. Tianyan, X. Zhang, G. Liu and G. Qiao, *Mater. Res. Bull.*, 2024, **180**, 113021.
26 C. Meng, Y. Cao, Y. Luo, F. Zhang, Q. Kong, A. A. Alshehri, K. A. Alzahrani, T. Li, Q. Liu and X. Sun, *Inorg. Chem. Front.*, 2021, **8**, 3007–3011.
27 J. Hou, Z. Huang, H. Lu, C. Chen, X. Wu, Y. Xiao, W. Wei, M. Xue, Y. Ma, X. Ma, S. Sun and D. Lin, *J. Mater. Chem. A*, 2025, **13**, 25042–25053.
28 W. Zhang, Y. Wang, L. Wang, Y. Li, H. Sun, C. Liu, Y. Wang, D. Zhang and J. Zhang, *Sci. Rep.*, 2025, **15**, 42694.
29 S. Arivuselvan, M. Elancheziyan, R. Atchudan, D. Ranjith Kumar, E. Sivasurya, S. Philomina Mary, P. Muthirulan, K. Won and M. Devaraj, *Heliyon*, 2024, **10**, e39241.
30 L. Malepe, D. T. Ndinteh, P. Ndungu and M. A. Mamo, *RSC Adv.*, 2022, **12**, 27094–27108.
31 J. Zhang, H. Guo, F. Yang, M. Wang, T. Zhang and H. Zhang, *ChemElectroChem*, 2022, **9**(2), e202101523.
32 F. Z. Kashani and M. Mohsennia in *International Journal of Hydrogen Energy*, Elsevier Ltd, 2025, vol. 101, pp. 348–357.
33 F. Zeraatkar and M. Mohsennia, *Int. J. Hydrogen Energy*, 2025, **101**, 348–357.
34 M. Arivazhagan, S. Prabu, M. Elancheziyan and J. Jakmunee, *Emergent Mater.*, 2025, **8**, 1067–1085.
35 H. Z. Yamani, Y. H. Hassan, N. Magdy, M. F. Abdel Ghany and M. M. Gomaa, *Microchim. Acta*, 2025, **192**, 374.
36 H. Wang, H. Zou, Y. Liu, Z. Liu, W. Sun, K. A. Lin, T. Li and S. Luo, *Sci. Rep.*, 2021, **11**, 1–11.
37 B. Selvaraj, J. B. B. Rayappan and K. J. Babu, *J. Alloys Compd.*, 2022, **914**, 165224.
38 Z. Wang, D. Zhang, M. Tang, Q. Chen, H. Zhang and X. Shao, *Sensor. Actuator. B Chem.*, 2023, **393**, 134141.
39 H. Sun, H. Huang, C. Hu, Y. Yan, Y. Hu, S. Guo and J. L. Chen, *Results Chem.*, 2022, **4**, 100306.
40 N. Amini and A. Maleki, *J. Electroanal. Chem.*, 2020, **877**, 114463.
41 M. Zar, H. Tabaian, H. Omidvar, A. S. Mehr and G. Hosseinzadeh, *J. Nanostruct.*, 2019, **9**, 539–546.
42 S. El-Akaad, R. Morozov, M. Golovin, O. Bol'shakov, S. De Saeger and N. Beloglazova, *Talanta*, 2022, **238**, 123025.
43 D. Kumar, N. Nesakumar, A. Jayalatha, J. Bosco and B. Rayappan, *Sensor. Actuator. B Chem.*, 2017, **248**, 708–717.
44 M. Faisal, J. Ahmed, M. M. Alam, M. Alsaiari, A. M. Asiri, R. H. Althomali, F. A. Harraz and M. M. Rahman, *Microchem. J.*, 2024, **200**, 110295.
45 B. Selvaraj, L. G. Priya and S. Balasubramanian, *RSC Adv.*, 2024, **14**, 35618–35627.
46 H. Yu, H. Wu, X. Tian, Y. Zhou, C. Ren and Z. Wang, *RSC Adv.*, 2021, **11**, 26963–26973.
47 N. Nataraj, P. Dash, R. Sakthivel, Y. C. Lin, H. W. Fang and R. J. Chung, *Chem. Eng. J.*, 2024, **485**, 149965.
48 X. Zhang, Y. Xu and B. Ye, *J. Alloys Compd.*, 2018, **767**, 651–656.
49 R. Mondal, S. F. Ahmed, N. Mukherjee and J. Inst, *J. Inst. Eng.*, 2024, **105**, 1361–1371.
50 J. A. Cruz-Navarro Jr, L. H. Mendoza Huizar, V. Salazar Pereda, J. A. Cobos Murcia and G. A. Álvarez Romero, *ECS Meet. Abstr.*, 2021, 2052.